A&A, 710, A97 (2026)
https://doi.org/10.1051/0004-6361/202557936

Astronomy & Astrophysics

A high-resolution study of the double radio relic system in MACS J1752.0+4440

M. Della Chiesa[1,2,⋆], A. Botteon[2], A. Bonafede[1,2], K. Rajpurohit[4,2], V. Cuciti[2], D. Hoang[3], R. J. van Weeren[5], X. Zhang[6], and F. Gastaldello[7]

[1] DIFA – Università di Bologna, via Gobetti 93/2, I-40129 Bologna, Italy
[2] INAF – IRA, via P. Gobetti 101, I-40129 Bologna, Italy
[3] Thüringer Landessternwarte, Sternwarte 5, 07778 Tautenburg, Germany
[4] Center for Astrophysics | Harvard & Smithsonian, 60 Garden Street, Cambridge, MA 02138, USA
[5] Leiden Observatory, Leiden University, PO Box 9513, 2300 RA Leiden, The Netherlands
[6] Max-Planck-Institut fur Extraterrestrische Physik, Giessenbachstrasse, 85748 Garching, Germany
[7] INAF – IASF Milano, via A. Corti 12, 20133 Milano, Italy

Received 1 November 2025 / Accepted 1 April 2026

ABSTRACT

Context. Radio relics are diffuse, extended synchrotron sources located in the outskirts of merging galaxy clusters. Their origin has been linked to shock waves injected into the intracluster medium, but the acceleration mechanism at the shock front remains under debate. Some clusters, such as MACS J1752.0+4440, host a double relics system, with two relics located on opposite sides of the cluster center.

Aims. To investigate the acceleration mechanism that generates radio relics, we studied the morphological and spectral properties of double relic system in MACS J1752.0+4440 ($z = 0.366$).

Methods. We present new wideband radio continuum observations obtained with uGMRT and JVLA, and previously published LOFAR data. We performed a detailed, high-resolution spectral analysis of the double relic system in MACS J1752.0+4440, and we observed and characterized substructures, particularly those of the brighter relic.

Results. We find a double-peaked surface brightness and spectral index profile for the NE relic and identify a "bright bar" substructure. Moreover, we observe surprisingly flat integrated spectral indices for both relics, at $\alpha_{\rm int}^{\rm NE} = -0.91 \pm 0.06$ and $\alpha_{\rm int}^{\rm SW} = -0.83 \pm 0.05$. We studied the spatial variation of the spectral index, observing a coherent trend with the observed substructures. We estimate injection Mach numbers of $\mathcal{M}_{\rm NE} = 3.1^{+0.1}_{-0.1}$ and $\mathcal{M}_{\rm SW} = 3.2^{+0.1}_{-0.1}$. We performed a spectral curvature analysis for both relics, generating color-color plots, and we observe two "concave" spectra characterized by positive spectral curvature, in contrast to particle population aging models.

Conclusions. The observed properties of the NE relic are not consistent with a simple scenario involving a single shock front and a single particle-injection event. Multiple shock surfaces, reacceleration, and projection effects likely play a role in shaping the morphology of the relic.

Key words. radiation mechanisms: non-thermal – galaxies: clusters: general – galaxies: clusters: intracluster medium – galaxies: clusters: individual: MACS J1752.0+4440 – large-scale structure of Universe – radio continuum: general

1. Introduction

Merging galaxy clusters can host several kinds of diffuse, large-scale synchrotron sources whose emission is not associated with individual cluster galaxies. These sources can be broadly classified into radio relics and radio halos (see van Weeren et al. 2019, for a review). Their presence reveals weak magnetic fields ($\sim$0.1−10 μG) and relativistic particles distributed on cluster scales as nonthermal components of the intracluster medium (ICM). Radio relics are megaparsec-sized synchrotron sources typically observed in the outskirts of galaxy clusters. They often show irregular arc-like morphologies, curved toward cluster center. The radio spectrum of the relics is steep, with $\alpha < -1$ (where the flux density $S_\nu \propto \nu^\alpha$), and it often steepens from the leading outer edge of the relic to the cluster center.

The origin of radio relics has been closely linked to shock waves injected into the ICM during merger events (Roettiger et al. 1999). Although the exact formation mechanism is not fully understood, it is believed that a small fraction of the kinetic energy dissipated during a cluster merger is channeled into nonthermal components (Brunetti & Jones 2014). The mechanism responsible for particle acceleration is believed to be diffusive shock acceleration (DSA) at merger shocks (see Bykov et al. 2019, for a review). However, several open questions remain about the viability of DSA. The main open question concerns the DSA efficiency, whose estimated value is insufficient to accelerate thermal particles and produce the radio power observed in most relics, given that radio relics are associated with weak shocks ($M < 3$; Botteon et al. 2020). Moreover, the nondetection of γ-ray emission from galaxy clusters, which is expected to result from collisions between accelerated cosmic-ray protons and thermal protons (Vazza & Brüggen 2014; Vazza et al. 2016), poses a challenge to the DSA model. Finally, the radio spectral indices of some relics are incompatible with the DSA predictions and stationary conditions, showing $\alpha > -1$ (i.e., Stuardi et al. 2022). Possible solutions to these problems include the presence of fossil relativistic electrons in the ICM, which can be further accelerated by DSA with lower efficiencies (Bonafede et al. 2014; Markevitch et al. 2005; Kang & Ryu 2016; van Weeren et al. 2017; Inchingolo et al.

⋆ Corresponding author: maicol.dellachiesa@inaf.it

2022)), or alternative acceleration processes (Zimbardo & Perri 2018; Kang et al. 2019).

The connection between relics and shocks has been confirmed by detecting surface-brightness distributions and temperature jumps at the positions of radio relics in X-rays (i.e., Sarazin et al. 2013; Shimwell et al. 2015; van Weeren et al. 2016; Botteon et al. 2016; Di Gennaro et al. 2019). Particularly interesting are the so-called double radio relics, in which two relics are found on diametrically opposite sides of the cluster center and are believed to trace two shock waves created in a binary and nearly head-on merger event (van Weeren et al. 2011). A modern broadband study on an ensemble of double relic galaxy clusters shows that the merger axis of these objects is preferentially oriented near the plane of the sky (Golovich et al. 2019).

High-resolution studies reveal filamentary emission in radio relics (i.e., Owen et al. 2014; Rajpurohit et al. 2020, 2022; de Gasperin et al. 2022; Chibueze et al. 2023). Although not easy to explain, this filamentary emission is expected and reproduced by magnetohydrodynamical simulations of cluster merger shocks (Vazza et al. 2012; Skillman et al. 2013; Wittor et al. 2019). Dominguez-Fernandez et al. (2021) show how 3D magnetohydrodynamical simulations of merger shocks reproduce radio relics whose radio emission is concentrated into threads and filaments in the shock plane. Their findings highlight key features that connect the observable characteristics of radio relics with the dynamical properties of the upstream ICM. Furthermore, they show that weak shocks ($\mathcal{M} \approx 2$) are unlikely to reproduce observable radio relics because they cannot modify the initial state of the pre-shock magnetic field. Moreover, Wittor et al. (2023) show that the observed and simulated filaments have similar properties and that their 3D structures are related to the magnetic field and Mach number distribution.

2. MACS J1752.0+4440

The MACS J1752.0+4440 galaxy cluster, located at $z = 0.366$, was reported as a candidate host for a double relic system by Edge et al. (2003) as part of the MAssive Cluster Survey (MACS; Ebeling et al. 2001). It was first observed in the radio band in the NRAO Very Large Array Sky Survey (NVSS; Condon et al. 1998) and Westerbork Northern Sky Survey (WENSS; Rengelink et al. 1997), which revealed two radio sources found on opposite sides of the cluster center.

van Weeren et al. (2012a) studied the cluster in the radio band with the WSRT (25, 21, 18, and 13 cm) and VLA (1.4 GHz) data. They detected a double relic system, with the two relics located northeast (NE) and southwest (SW) of the cluster center, together with a radio halo component. They obtained spectral indices of $\alpha = -1.16 \pm 0.03$ and $\alpha = -1.10 \pm 0.05$ for the NE and SW relic, respectively, through an integrated spectral analysis. Bonafede et al. (2012) produced spectral index images of the cluster using WSRT (18 cm) and GMRT (325 MHz) observations, highlighting a clear steepening of the spectral index in the NE relic from the cluster periphery toward the cluster center. The SW relic shows a gradient of the spectral index along its main axis. Bonafede et al. (2012) studied the radio polarization of the two relics and found that they are highly polarized, with polarization values reaching up to 40% in the external regions of the relics. The high level of polarization suggests an ordered magnetic field at the relic positions. By comparing the observed radio and X-ray morphologies of MACSJ1752.0+4440 with cosmological simulations, they showed that a binary cluster merger, with realistic

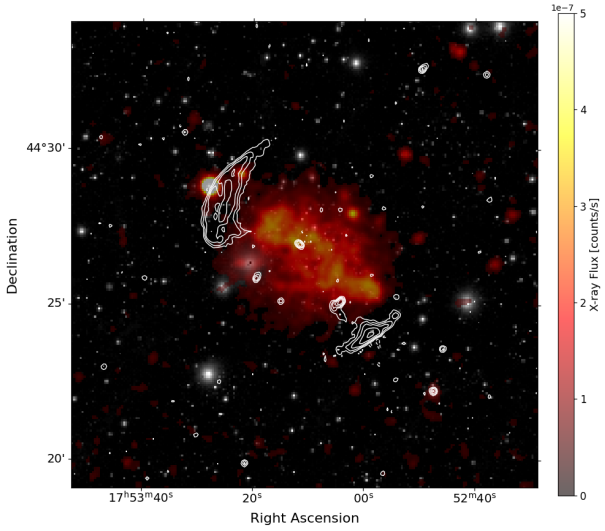

Fig. 1. Composite image of MACS J1752.0+4440. The LOFAR 144 MHz contours (white) are overlaid onto an optical image from Pan-STARRS (gray) and an X-ray image from XMM-Newton (red) from (Botteon et al. 2022; Zhang et al. 2023).

assumptions on shock- and turbulence-driven particle acceleration, can successfully reproduce the observed features in both morphology and radio power. Finally, MACS J1752.0+4440 belongs to the sample of Planck Sunyaev Zel'dovich detected sources (PSZ2 G071.21+28.86; Planck Collaboration XXVII 2016). These clusters are covered in the second data release of the LOw Frequency ARray (LOFAR) Two-meter Sky Survey (LoTSS-DR2; Shimwell et al. 2022), analyzed by Botteon et al. (2022). (Jones et al. 2023) report on the analysis of the relics in that sample.

The optical and X-ray study by Finner et al. (2021) reveals key characteristics of MACS J1752.0+4440. By modeling each subcluster with a Navarro-Frenk-White (NFW; Navarro et al. 1997) halo, they estimate a 1:1 mass ratio merger, with a total mass of $M_{200} = 14.7^{+3.8}_{-3.3} \times 10^{14}\, M_{\odot}$. In addition, a spectral analysis by Golovich et al. (2019) suggests a head-on major merger along the plane of the sky, with a time since collision of 0.9 ± 0.1 Gyr. X-ray observations show two gas clumps at a projected distance of 1.2 Mpc, which supports the dynamical state of the system (Fig. 1). An X-ray surface brightness analysis by Finner et al. (2021) shows two peaks connected by a bridge of emission, consistent with a small impact parameter. The two X-ray brightness peaks coincide with cold fronts. However, the available X-ray data were not sufficiently deep to detect a shock front in the cluster outskirts.

In this work, we present the results of new observations of the MACS J1752.0+4440 galaxy cluster, combining data from the upgraded Giant Metrewave Radio Telescope (uGMRT), the Karl G. Jansky Very Large Array (JVLA), and LOFAR. These observations achieve high resolution, allowing us to observe and characterize substructures in radio relics within the galaxy cluster in great detail.

The structure of this paper is as follows. Section 3 presents a summary of the observations and details of the data reduction process. Section 4 presents the newly obtained radio images and the associated spectral analysis. Section 5 presents an explanation of the observed findings. Finally, Section 6 summarizes the analysis.

Table 1. Observation parameters.

	LOFAR	uGMRT Band 3	uGMRT Band 4	JVLA
Bandwidth	48 MHz	200 MHz	200 MHz	1 GHz
Central Frequency	144 MHz	416 MHz	650 MHz	1600 MHz
Observation dates	June 16, 2019	June 14, 2021	August 1, 2021	June 19, 2012
Total on-source time	8 h	5 h	5 h	15 h
Configurations				B, C, D

Table 2. Imaging parameters.

Frequency	Restoring beam	Smoothed beam	# of channels	Briggs	uv-cut	RMS noise [μJy/beam]	RMS noise at 7″ [μJy/beam]
144 MHz	$6.5'' \times 4.1''$	7″	6	–1	$\geq 0.15k\lambda$	150	280
416 MHz	$5.4'' \times 4.6''$	7″	5	–1	$\geq 0.15k\lambda$	34	70
650 MHz	$3.2'' \times 2.8''$	7″	4	–1	$\geq 0.15k\lambda$	17	23
1.6 GHz	$3.2'' \times 3.0''$	7″	3	+0.5	$\geq 0.15k\lambda$	10	15

Throughout this paper, we assume a Λ Cold Dark Matter cosmology with $H_0 = 72\,\mathrm{km\,s^{-1}\,Mpc^{-1}}$, $\Omega_m = 0.27$, and $\Omega_\Lambda = 0.73$. At the cluster redshift, 1″ corresponds to a physical scale of 4.98 kpc. All output images are in the J2000 coordinate system and are corrected for primary beam attenuation.

3. Observations and data reduction

3.1. uGMRT

MACS J1752+4440 was observed in June 2021 in band 3 (300–500 MHz) and band 4 (550–750 MHz) for a total of five hours in each band, bookended by ten-minute calibrator scans (3C286). Both band 3 and band 4 observations span a 200 MHz frequency range. We split the band 3 dataset into six 33.3 MHz slices and band 4 into four 50 MHz slices. During the analysis of the individual frequency slices, we detected a significant level of radio frequency interference (RFI) in the lowest-frequency slice of band 3. Due to the severity of the contamination, we excluded this slice from further analysis.

We processed each slice independently using the Source Peeling and Atmospheric Modeling (SPAM; Intema et al. 2009) pipeline, which measures ionospheric phase errors toward the strongest sources in the field of view, allowing the derivation of direction-dependent gains and fitting of a phase screen over the entire field of view. We carried out the final analysis by jointly imaging the slices of each observing band.

3.2. JVLA

We observed MACS J1752+4440 with the JVLA L band (1–2 GHz) in three different configurations: D, C, and B, for a total of 15 hours, bookended by ten-minute calibrator scans. Each observation comprised 11 spectral windows of 64 channels in full polarization, for a final bandwidth of 600 MHz, reduced from the nominal band due to flagging. We recorded all four polarizations (RR, RL, LR, and LL). We precalibrated the data using selfcalibration in `CASA`, flagging with `AOFlagger`, and applying standard flux and bandpass calibration. We provide details of the observations in Table 1.

3.3. LOFAR

MACS J1752.0+4440 was observed as part of LoTSS (Shimwell et al. 2017, 2019, 2022) with LOFAR High Band Antenna (LOFAR HBA). We reduced and calibrated the data using the LoTSS DR2 pipeline Tasse et al. (2021), followed by an "extraction and selfcalibration" scheme (van Weeren et al. 2021). We used the data calibrated in Botteon et al. (2022) to produce new radio images, which we combined with the new uGMRT and JVLA data. Botteon et al. (2022) provide a detailed description of the reduction process.

3.4. Imaging

We used `WSclean` (Offringa et al. 2014) for the deconvolution process. We produced high-resolution images using a robust weighting of +0.5 for the VLA band and –1 for all other telescopes. We used the multiscale and multifrequency deconvolution technique (Offringa & Smirnov 2017) to image the dataset, dividing the total bandwidth into narrower frequency channels and interpolating across them to produce high-fidelity radio images. To speed up and improve the cleaning process, we produced masks for each image using the `breizorro` software[1]. We chose the mask thresholds using `breizorro` with different threshold values, selecting the value that best represents the relics. Table 2 provides a summary of the imaging parameters. We corrected images for primary beam attenuation using a cosine beam shape (Condon & Ransom 2016).

Since spectral analysis relies on comparisons between images at different frequencies, it is crucial that images from different interferometers sample the same range of angular scales. Therefore, we imaged our data with a common lower *uv*-cut at 150λ, which corresponds to the shortest well-sampled baseline in the JVLA dataset. This minimizes differences in spatial sensitivity between datasets, ensuring more reliable and self-consistent spectral comparisons. We convolved the images to a common restoring beam of 7″, forcing a circular beam, using the `imsmooth` tool in `CASA`. Finally, we verified the consistency of the integrated flux densities between the original full-resolution

[1] https://github.com/ratt-ru/breizorro

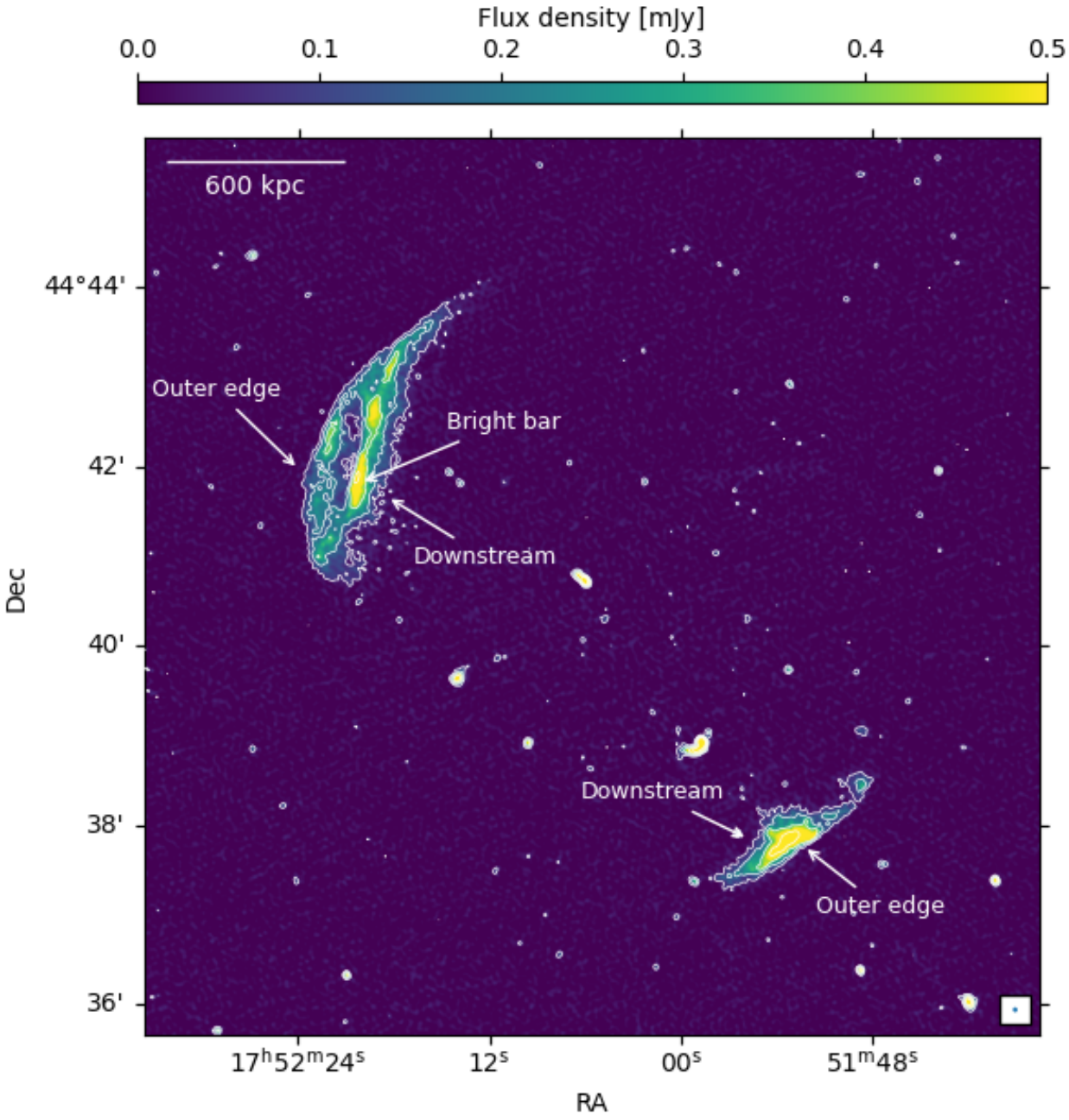

Fig. 2. Band 4 (650 MHz) uGMRT image of MACS J1752+4440. This image, with a resolution of $3'' \times 3''$, is the highest resolution image obtained so far for this cluster. The different structures are labeled in white. The outer edge component outlines the possible position of the merger shock that generated the NE relic, and the bright bar is a substructure present in the downstream region of the first component. The SW relic shows no substructures at this resolution. Contours start at $3\sigma_{\rm rms}$ and are separated by a factor of two. The beam and scale bar are shown at the bottom and top of the image, respectively.

maps and the convolved $7''$ images to ensure flux conservation during the smoothing process.

We estimated the uncertainty in the flux-density measurement as

$$\Delta S = \sqrt{(\sigma_{\rm rms})^2 N_{\rm beam} + (f \cdot S)^2}, \quad (1)$$

where $\sigma_{\rm rms}$ is the rms noise, $N_{\rm beam}$ is the number of beams covered by the source, f is the absolute flux density calibration uncertainty, and S is the flux density. We assumed an absolute flux density uncertainty of 10% for LOFAR (Shimwell et al. 2022), 5% for uGMRT bands 3 and 4 (Chandra et al. 2004), and 2.5% for JVLA data (Perley & Butler 2013).

4. Results

Figure 2 shows the deep $3''\times3''$ resolution uGMRT band 4 image of MACS J1752.0+4440. The high resolution of the image allowed us to resolve the fine details of the two radio relics. In particular, the northeast (NE) relic shows a substructure along its width. We divided the NE relic into three components: the "outer

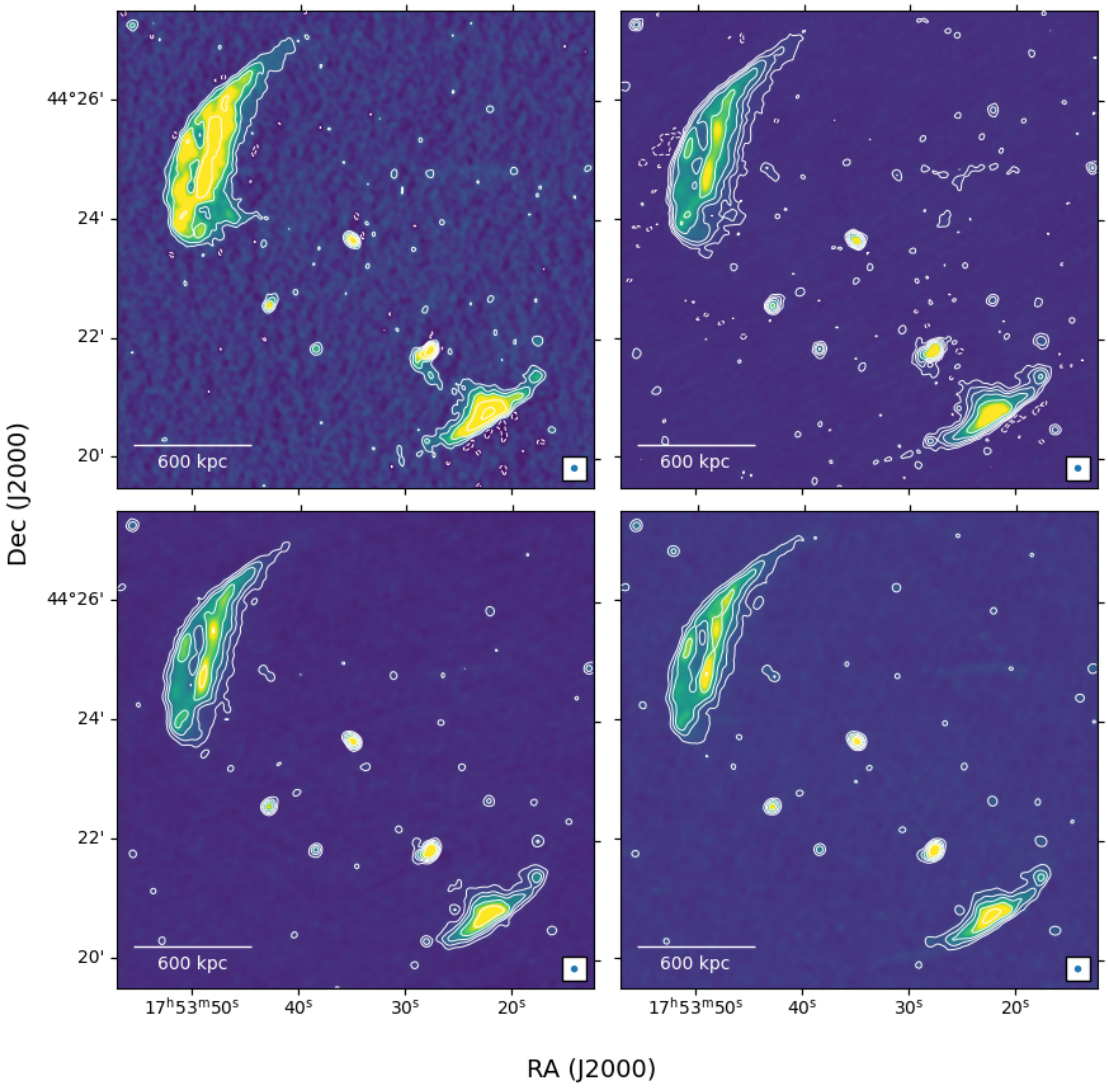

Fig. 3. Radio images of the MACS J1752+4440 cluster at 7″ resolution. Top Left: LOFAR image at 144 MHz with noise of $\sigma_{\rm rms,144}$ = 280 μJy beam^{-1}. Top Right: uGMRT image at 416 MHz with noise of $\sigma_{\rm rms,416}$ = 70 μJy beam^{-1}. Bottom Left: uGMRT image at 650 MHz with noise of $\sigma_{\rm rms,650}$ = 23 μJy beam^{-1}. Bottom Right: JVLA image at 1.6 GHz with noise of $\sigma_{\rm rms,1600}$ = 15 μJy beam^{-1}. Images have a common angular resolution of 7″ × 7″ and contour levels are drawn at $[-3, 3, 9, 18, 36, 72] \times \sigma_{\rm rms}$; the negative contour is shown as a dashed line. The color scale is logarithmic, and beam and scale bar are shown at the bottom of the images.

edge" at the expected position of the shock wave, the "bright bar" located in the middle of the relic's width, and a "downstream" region toward the cluster center. The outer edge and the bright bar are located at ≈1 Mpc and 0.9 Mpc from the cluster center, respectively, where the cluster center is defined as the midpoint of the axis connecting the two relics. The same features appear in 7″ resolution images at each frequency (see Fig. 3).

The two relics have largest linear sizes (LLSs) of $\mathcal{L}_{\rm NE}$ = 1.3 Mpc and $\mathcal{L}_{\rm SW}$ = 0.7 Mpc.

We selected two regions surrounding the two radio relics, guided by the LOFAR $3\sigma_{\rm rms}$ contours at a resolution of 7″, as shown in the right of Fig. 4. After verifying that no contaminating radio sources were present, we measured the two integrated flux densities of the two relics at each frequency. The left panel of Fig. 4 shows that the observed radio spectra over the considered frequency range are well represented by a power-law fit. We report the results in Table 3.

This fit yields two integrated spectral indices, $\alpha_{\rm int}^{\rm NE} = -0.91 \pm 0.06$ and $\alpha_{\rm int}^{\rm SW} = -0.83 \pm 0.05$. These values differ from those reported in previous studies (van Weeren et al. 2012a; Bonafede et al. 2012), which were based on data with a lower-resolution and narrower frequency. The improved resolution of our data allowed us to calculate the spectral index over regions accurately tracing the edges of the radio relics, while the wider frequency range and greater sensitivity enabled more precise measurements of the integrated radio flux densities.

4.1. Spectral profiles

Given their origin, radio relics typically exhibit synchrotron emission that peaks at the shock front and follows a power-law distribution in both the particle energy and the radio spectrum Hoeft & Brüggen (2007). After the shock passage, particle populations undergo aging, radiating energy through synchrotron and inverse Compton losses. Higher-energy particles, which are responsible for higher-frequency emission, age faster, producing a steepening of the power law at high frequencies in the radio spectrum. We compared the properties of the relics in MACS

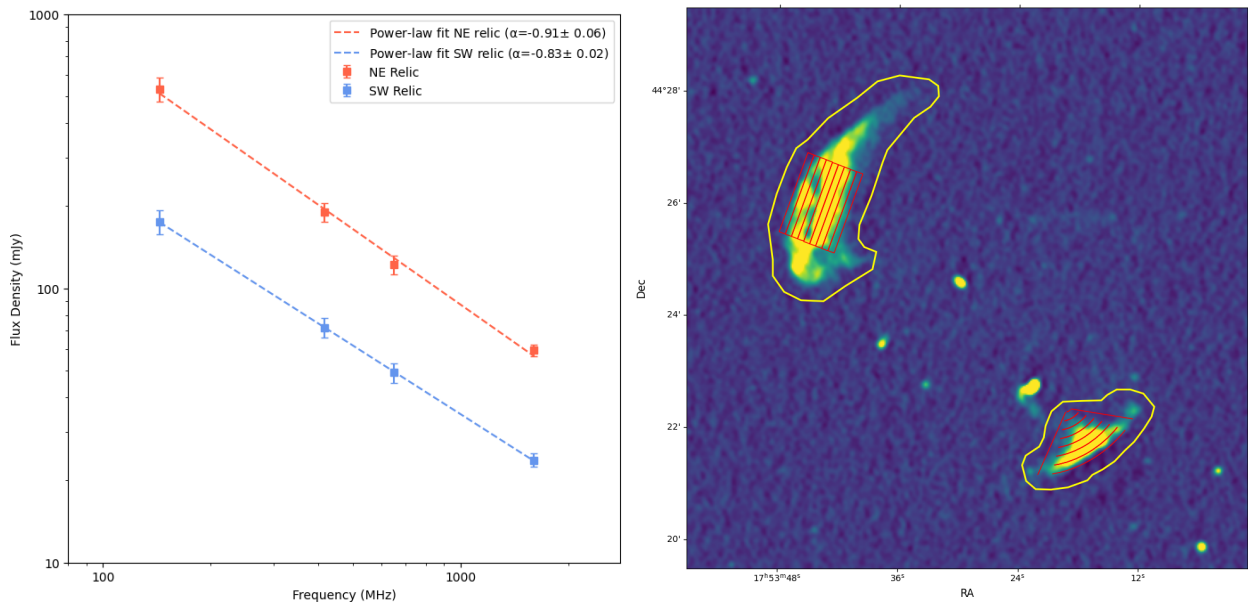

Fig. 4. Left: Spectra for the NE (red) and SW (blue) relic, fitted by two power laws. Right: High-resolution LOFAR continuum image at 144 MHz with the regions used to estimate the flux density of the two relics overlaid in yellow. In addition, the regions used to produce the brightness and spectral index profiles are overlaid in red along the relics.

J1752+4440 with the DSA predictions by analyzing their surface brightness and spectral index properties. In the simplest idealized case, a merger-driven shock with electrons injected at the shock would generate a radio relic with a surface brightness profile that peaks at the shock front and decreases toward the cluster center. Numerical simulations of shocks that generate radio relics (Domínguez-Fernández et al. 2021; Wittor et al. 2023) show a more complex scenario. In fact, the increasing resolution of simulations and radio observations (Rajpurohit et al. 2020; Chibueze et al. 2023) of radio relics confirms the presence of substructures and filaments downstream of these objects. The bright bar feature observed in the NE relic of MACS J1752 could further support the complex structure of the relics.

We produced surface brightness and spectral index profiles along regions selected on the relics' major axes. We defined these regions using boxes with a width of 7″, equal to the beam size (right panel of Fig. 4). Fig. 5 shows the brightness profile at7″ resolution for both relics. In the NE relic (Fig. 5, left), the profile reveals a distinct local maximum that spatially coincides with the bright bar substructure. Beyond this feature, the emission maintains a constant value toward the outer edge of the relic. This profile highlights the peak brightness in the region behind the position of the outer edge. In an idealized single-shock scenario producing particle (re-)acceleration with homogeneous properties of the downstream medium, the expected spectral index profile of a radio relic shows a monotonic decrease, with the flattest spectra at the merger shock and steepening toward the cluster center.

To study the origin and infer the spectral properties of the radio emission of the two relics, we produced spectral index profiles at high and low frequencies.

We computed the spectral index using the general equation

$$\alpha = \frac{\log\left(\frac{S_1}{S_2}\right)}{\log\left(\frac{\nu_1}{\nu_2}\right)}, \quad (2)$$

where S_1 and S_2 are the measured flux densities at frequencies ν_1 and ν_2. In Fig. 6, we compare the spectral indices calculated between LOFAR (144 MHz) and uGMRT band 3 (416 MHz), as well as with uGMRT band 4 (650 MHz) and JVLA (1.6 GHz). The NE relic profiles reveal a nonlinear trend, with the flattest spectral index coinciding with the position of the outer edge and a flattening in the central regions. The SW profile instead shows a gradual steepening of the spectral index without features in the profile. Although the bright bar morphology in the NE relic was visually distinguishable in previous low-resolution studies (i.e., van Weeren et al. 2012a), it remained unresolved for a detailed quantitative analysis. In this work, our higher resolution allows us to move beyond visual inspection. The profiles presented in Fig. 5 provide a characterization of the surface brightness and spectral index properties of this substructure.

Table 3. Measured flux densities at four frequencies for the NE and SW relics, and the integrated spectral index.

	Frequency [MHz]	Flux density [mJy]	$\alpha_{\rm int}$
NE	144	530 ± 50	−0.91 ± 0.06
	416	203 ± 20	
	650	130 ± 10	
	1600	62 ± 30	
SW	144	177 ± 18	−0.83 ± 0.05
	416	79 ± 6	
	650	56 ± 4	
	1600	26 ± 1	

4.2. Spectral index map

We investigated the influence of the bright bar substructure on the spatial variation of the spectral index across the two relics by producing a pixel-to-pixel spectral index map (Fig. 7). Across both relics, the spectral index ranges from roughly $\alpha \sim -0.6$ to -1.4. Notably, although the SW relic shows uniform steepening along its minor axis, the bright bar substructure in the

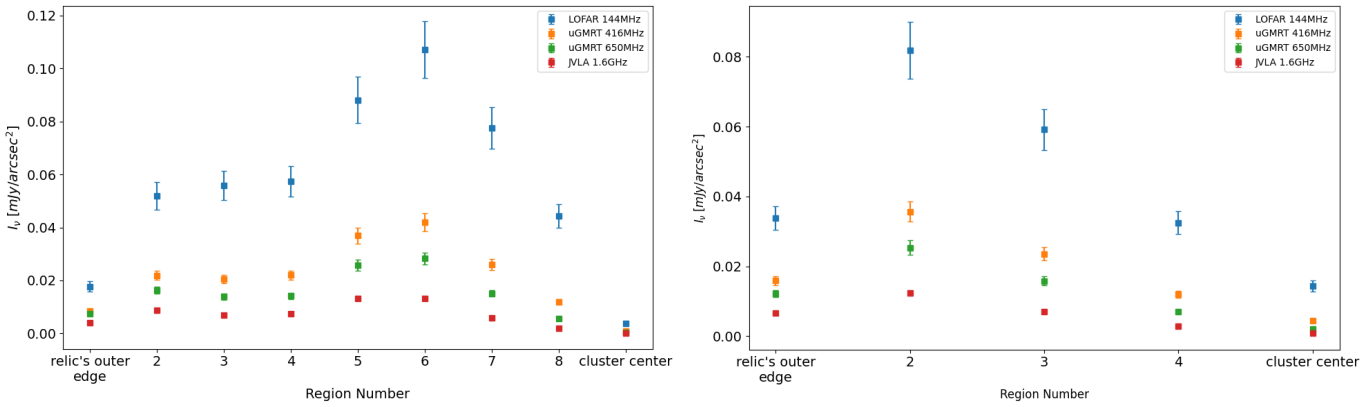

Fig. 5. Surface brightness profiles for the two radio relics. Left: Profile of the NE relic. Peak brightness occurs region five and six, with a second peak in region three. This is consistent with the spectral index profiles, which also show two peaks at the position of the two substructures of the relic. Right: Profile of the SW relic. Peak brightness occurs in region two, followed by a rapid decline in the downstream region.

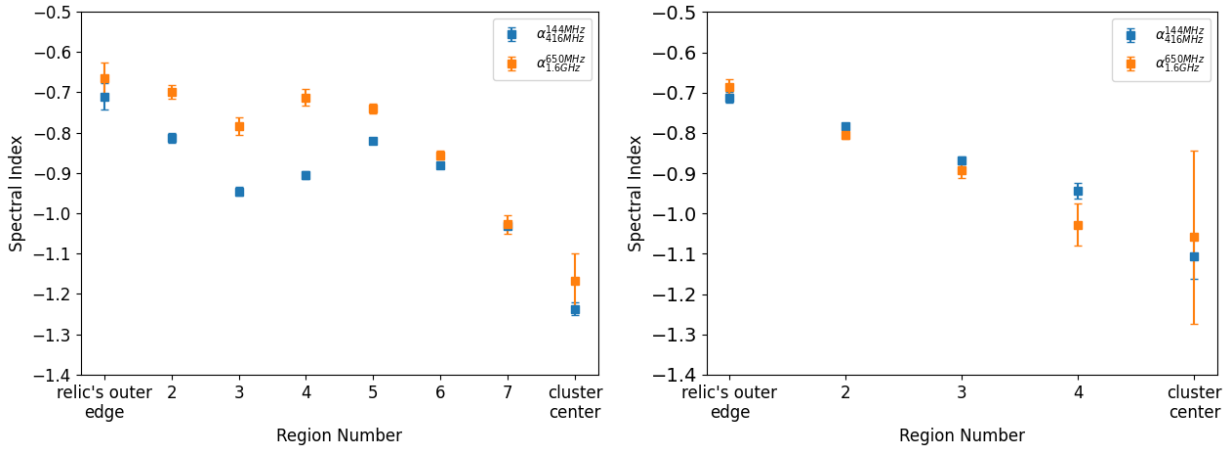

Fig. 6. Spectral index profiles, calculated in the two frequency ranges, at high-resolution. Left: Profiles for the NE relic. The low-frequency profile shows two peak in spectral index, one at the position of the merger shock and one at the position of the substructure. The high-frequency profile differs, showing a flat behavior along the regions overlaid on the bright bar substructure. Both profiles show a sharp drop of spectral index into downstream regions. Right: Profiles for the SW relic. Both profile show a similar trend, decreasing toward the cluster center.

NE relic is clearly recovered in the spectral index map with flatter values ($\alpha \sim -0.6$ to -0.8). This behavior likely reveals information about the origin of the relic. We discuss this in Section 4.

4.3. Mach numbers

The DSA model for particle acceleration is commonly used to describe particle acceleration in astrophysical shocks, which are believed to generate radio relics. In this scenario, considering a power-law energy distribution of relativistic electrons $n_E \propto E^{-\delta}$, the slope δ is related only to the shock's strength as

$$\delta_{\rm inj} = 2\frac{\mathcal{M}^2+1}{\mathcal{M}^2-1}. \quad (3)$$

Under stationary conditions, assuming that the physical conditions in the downstream regions do not change significantly with distance from the shock front, the integrated electron spectrum follows a power law with slope $\delta = \delta_{\rm inj} + 1$. Using the relation between the energy distribution and the radio spectral index, $\alpha = (1-\delta)/2$, we can directly connect the integrated radio spectral index to the Mach number as

$$\alpha_{\rm int} = -\frac{\mathcal{M}^2+1}{\mathcal{M}^2-1}. \quad (4)$$

In the downstream region, radiative cooling of the electrons leads to a progressively steepening electron spectrum. When considered over a distance exceeding the electron cooling length, the spectral index of the integrated spectrum can be expressed as

$$\alpha_{\rm inj} = \frac{1}{2} - \frac{\mathcal{M}^2+1}{\mathcal{M}^2-1} = \frac{1}{2} + \alpha_{\rm int}. \quad (5)$$

As the integrated spectral index of both MACS J1752+4440 relics is $\alpha_{\rm int} > -1$, the Mach number cannot be calculated through Eq. (4), suggesting a more complex scenario than outlined above.

However, assuming that we observe the injected electron population, we estimate the Mach number from the injection spectral index of the shock, $\alpha_{\rm inj}$, defined as the spectral index measured in the outermost regions tracing the shock position. Table 4 shows the results for both radio relics and both resolutions.

4.4. Spectral curvature

As merger-shock models predict increasing spectral curvature in post-shock regions, and given the peculiar structure of the MACS J1752+4440 relics, we analyzed their spectral curvature.

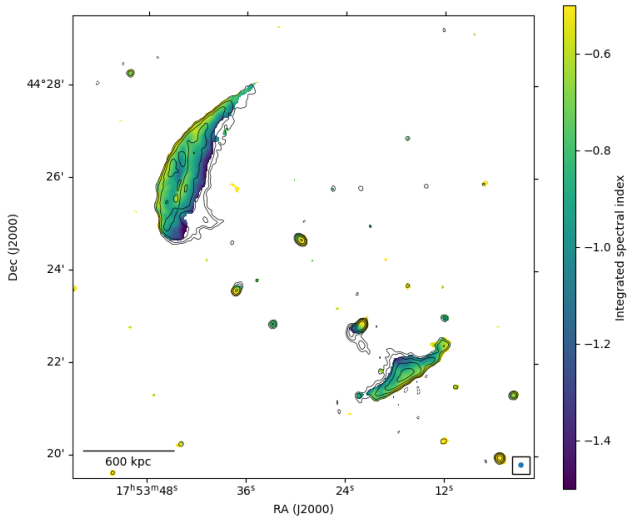

Fig. 7. Spectral index map, obtained from fitting the four measurements in each pixel above the $3\sigma_{\rm rms}$ level. Contours are drawn from the LOFAR 144 MHz image, starting at the $3\sigma_{\rm rms}$ level and spaced by factors of two.

Table 4. Spectral indices and Mach numbers of the two radio relics.

	$\alpha_{\rm inj}$	$\mathcal{M}_{\rm inj}$	$\alpha_{\rm int}$
NE	-0.74 ± 0.02	$3.1^{+0.1}_{-0.1}$	-0.91 ± 0.06
SW	-0.71 ± 0.01	$3.2^{+0.1}_{-0.1}$	-0.83 ± 0.05

Notes. Integrated Mach numbers cannot be calculated and so are not present.

We employed the color-color diagram technique (Rudnick et al. 1994; van Weeren et al. 2012b) which consists of comparing the spectral index calculated between a low (LOFAR 144 MHz – uGMRT band 3 416 MHz) and high (uGMRT band 4 650 MHz – JVLA 1.6 GHz) frequency range, calculated on a grid of beam-sized (7″) boxes covering the two radio relics (see Fig. 8).

Color-color diagrams provide information on the curvature of the spectrum, and thus on particle aging, by comparing the position of the points with respect to a perfect power-law line (i.e., the injection spectrum), which corresponds to $\alpha^{\nu_1}_{\nu_2} = \alpha^{\nu_3}_{\nu_4}$.

We considered only the boxes in which the integrated flux density is above $3\sigma_{\rm rms}$ in all images simultaneously. Although this guarantees a high signal-to-noise ratio and avoids contamination by noise, it introduces selection biases. Specifically, this threshold preferentially excludes low-surface-brightness regions, which are typically associated with older, steeper-spectrum emission. Fig. 9 shows the color-color plots for both relics.

In both relics, and notably in the NE relic, we observe points closely following the power-law line. This behavior may be attributed to several factors, including fresh or reaccelerated electron populations at multiple sites, or projection effects, where particle populations of different radiative age overlap along the line of sight (Wittor et al. 2023). This behavior suggests that a scenario involving a single shock front moving exactly in the plane of the sky is oversimplified. As a simple comparison, we plotted a Jaffe-Perola (JP; Jaffe & Perola 1973) model with an injection spectrum of –0.5 together with the observed curvature points. The JP model assumes a single burst of particle acceleration and an isotropic angle between the magnetic field and the electron velocity vectors (the so-called pitch angle), on a timescale shorter than the radiative timescale. It is commonly used for post-shock regions, assuming a planar shock front, observed perfectly edge-on (Rajpurohit et al. 2020, 2021). The observed curvature points are not represented by the JP model. Other models have been considered in the literature that take into account a slight inclination along the line of sight for the shock front (i.e., KGJP; Komissarov & Gubanov 1994), but since the trend is similar to that produced by the JP model, we did not plot them.

5. Discussion

The detection of an integrated spectral index flatter than –1 in MACS J1752 is highly significant, as it represents a deviation from the typical population of radio relics. In addition to Abell 3365 (Duchesne et al. 2021), MACS J1752 is one of the few well-documented cases in which the integrated spectrum challenges the fundamental injection limits of standard DSA models. Historically, other candidates were proposed, but subsequent observations generally showed consistency with standard DSA predictions. For instance, while van Weeren et al. (2009) initially reported $\alpha > -1$ for ZwCL 2341.1+0000, a recent analysis by Zhang et al. (2021) using GMRT and JVLA data yields significantly steeper indices. Similarly, (Hindson et al. 2014; Riseley et al. 2015) initially reported flat values for Abell 3667. By contrast, using in-band MeerKAT data, de Gasperin et al. (2022) found spectral indexes <-1 for both relics. However, combining the MeerKAT measurement with literature data, they found alpha <-1 for the NW relic and >-1 for the SE relic.

Furthermore, advances in state-of-the-art observational techniques with progressively increasing resolution have led to more frequent detections of substructures within radio relics, such as that observed in the NE relic of MACS J1752. For example, filamentary structures and twisted ribbons have recently been observed in numerous radio relics (Rajpurohit et al. 2020; de Gasperin et al. 2022; Chibueze et al. 2023; Rajpurohit et al. 2024). The physical processes governing the nature of these features are still unclear. In fact, the bright bar component of the NE relic and the trends in surface brightness and spectral index cannot be explained by an isolated, uniform shock surface. To gain deeper insight into the underlying physical mechanisms, we investigated the potential presence of multiple particle populations with different radiative ages along the NE relic structure. We plotted the spectral index calculated between LOFAR 144 MHz and JVLA 1.6 GHz against the LOFAR 144 MHz flux density using the same boxes shown in Fig. 8, color-coding the points based on the position of the box along the relic. In Fig. 10, we observe that the outer edge spans low to moderate radio fluxes with consistently flat spectra, typical for freshly accelerated electrons. In contrast, the bright bar shows higher fluxes but steeper spectral indices. To quantify the change in spectral index between the two regions, we calculated the average spectral index between the outer edge and the bright bar points. We obtain $\langle\alpha_{\rm edge}\rangle = -0.76 \pm 0.02$ and $\langle\alpha_{\rm bar}\rangle = -0.94 \pm 0.02$, corresponding to a decrease in the average spectral index of -0.18. The downstream region shows a lower flux density and spectral index than both the main shock and the filament. A simple, uniform shock scenario cannot account for the observed trends and the observed spectral indices, which suggest a more complex physical picture. For example, a complex shock surface could

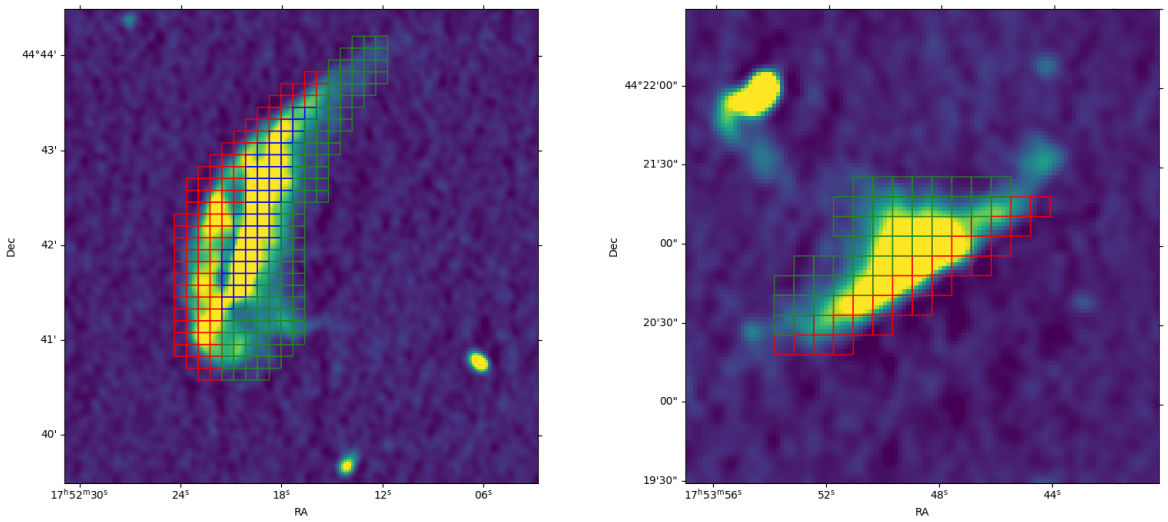

Fig. 8. Zoom-in view of the NE and SW radio relics, with selected regions for the curvature study overlaid in different colors. The three components of the NE relic are divided as follows: red outlines the position of the outer edge, blue traces the bright bar, and green marks the downstream regions. Similarly, the shock front and the downstream regions are selected along the SW relic. The same colors are used to represent the structures in the following plots.

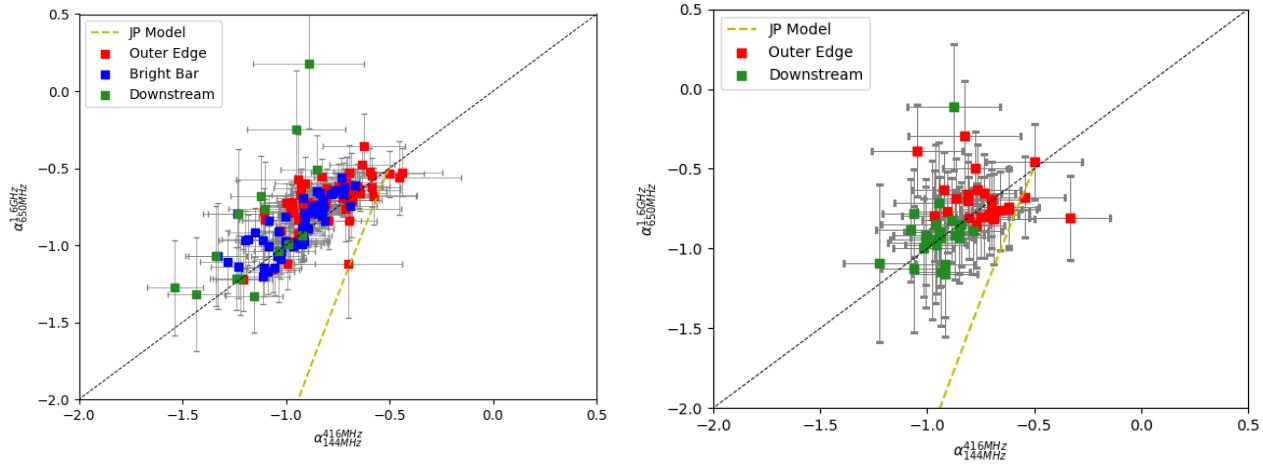

Fig. 9. Color-color plot for the two radio relics at high-resolution (7″). Left: Few points of the NE relic lie below the power-law line, consistent with a mostly power-law spectrum; some extend into the "concave" spectrum region. The coloring shows how the outer edge and the bright bar both fall mostly on the power-law line, with no sign of spectral steepening. Right: SW relic shows steepening at lower spectral indices, but still presents multiple points representing a flattening spectrum.

accelerate particles through repeated DSA events throughout the radio relic, leading to flat spectral indices. Similarly, projection effects could blend freshly accelerated particles with the downstream medium along the line of sight, producing flatter indices and influencing the morphology of the observed radio emission. Moreover, magnetic field inhomogeneities may enhance radio emission in different regions of the relic.

Their highly polarized radio emission suggests that radio relics are primarily viewed edge-on (Ensslin et al. 1998), which would confine the merger axis to a direction near the plane of the sky. Simulations (Skillman et al. 2013) also show the same effect. Therefore, we expect the projection effect in clusters hosting radio relics to be minimized. Nevertheless, local projection effects at the location of the radio relic could reproduce the observed bright bar feature (Wittor et al. 2019). Furthermore, Domínguez-Fernández et al. (2024) show that the Mach number distribution of the shock front plays the primary role in shaping the observed surface brightness of radio relics. The substructure could also result from adiabatic compression induced by a secondary shock, which increases the maximum synchrotron frequency emitted by a population of fossil electrons by a multiple of the compression factor. However, the resulting boost is typically moderate (a factor of ~2), and the scenario has been ruled out in most shock cases (Hoang et al. 2018).

We did not identify any distinct features in the SW relic. Nevertheless, as discussed in Section 3, its spectral index remains flatter than expected from standard DSA models. This discrepancy may be attributed to projection effects or to a scenario in which the shock reached the SW region at a later stage, leading to spectral flattening.

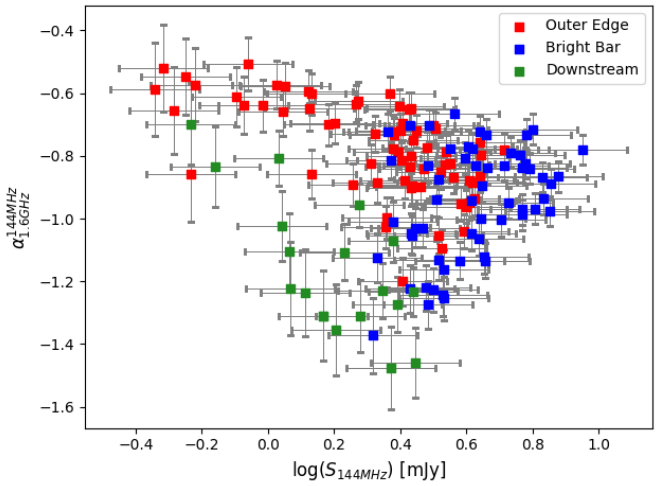

Fig. 10. Spectral index versus LOFAR 144 MHz flux density. The spectral index is calculated between LOFAR 144 MHz and JVLA 1.6 GHz data to leverage the broadest available frequency range. The high resolution of the images allows identification of the two substructures of the NE relic.

6. Summary and conclusions

We present results from deep, wide-band uGMRT band 3 (300–500 MHz) and band 4 (550–750 MHz) radio observations of the galaxy cluster MACS J1752.0+4440. We paired these observations with archival JVLA L band (1.6 GHz) data and LOFAR HBA data (Botteon et al. 2022, LoTSS-DR2) to perform a detailed spectral study of the cluster. The high resolution of these observations allowed us to observe and characterize the features in the radio relics of MACS J1752. We summarize our results as follows:

1. The radio emission from the two radio relics closely follows a power law, with integrated spectral indices of $\alpha^{\rm NE}_{\rm int} = -0.91 \pm 0.06$ and $\alpha^{\rm SW}_{\rm int} = -0.83 \pm 0.05$, and shows no signs of spectral steepening. These values are higher than typically expected for radio relics and flatter than predicted by simple DSA, indicating that a more complex and realistic scenario must be considered.
2. We detect a substructure along the NE relic, which we refer to as the "bright bar", across all radio bands. We observe no substructures along the SW relic.
3. We produced brightness and spectral index profiles for both relics. The NE relic peaks in surface brightness at the position of the bright bar and shows a secondary peak in spectral index at the same position. The SW relic shows peaks in both brightness and spectral index close to the relic edge, followed by a sharp decrease toward the cluster center.
4. A spectral-index curvature study shows that the spatial variation of the spectral index follows the relic substructures. Using color-color plots, we observe two spectra that closely follow a power law, with no clear signs of spectral curvature. This suggests either localized reacceleration, spatial mixing of multiple electron populations with different ages, or shock-induced compression of fossil plasma.
5. We investigated the nature of the bright bar substructure. We investigated the distribution of spectral indices and fluxes of several points along the NE relic, motivated by the hypothesis of a more complex scenario. This reveals two distinct radio-emitting structures corresponding to the outer edge and the bright bar substructures, suggesting a complex scenario.

In summary, our results highlight the crucial role of high-resolution radio observations in unveiling the intricate substructures within radio relics. The detection of such substructures in this work and in other recent studies provides compelling observational evidence that challenges the validity of a simple scenario in which a single shock front accelerates particles via DSA, instead pointing toward a more complex picture of particle acceleration and shock dynamics in the ICM. Future studies of polarization, particularly through rotation measure synthesis, are essential to probe the magnetic field orientation and to shed light on the physical origin of the observed substructures.

Acknowledgements. M. Della Chiesa acknowledges support from the ERC Consolidator Grant ULU 101086378. A. Bonafede acknowledges support from the ERC-CoG ***B***ELOVED, GA n. 101169773. LOFAR (van Haarlem et al. 2013) is the LOw Frequency ARray designed and constructed by ASTRON. It has observing, data processing, and data storage facilities in several countries, which are owned by various parties (each with their own funding sources), and are collectively operated by the ILT foundation under a joint scientific policy. The ILT resources have benefitted from the following recent major funding sources: CNRS-INSU, Observatoire de Paris and Université d'Orléans, France; BMBF, MIWF-NRW, MPG, Germany; Science Foundation Ireland (SFI), Department of Business, Enterprise and Innovation (DBEI), Ireland; NWO, The Netherlands; The Science and Technology Facilities Council, UK; Ministry of Science and Higher Education, Poland; Istituto Nazionale di Astrofisica (INAF), Italy. This research made use of the Dutch national e-infrastructure with support of the SURF Cooperative (e-infra 180169) and the LOFAR e-infra group, and of the LOFAR-IT computing infrastructure supported and operated by INAF, including the resources within the PLEIADI special "LOFAR" project by USCC of INAF, and by the Physics Dept. of Turin University (under the agreement with Consorzio Interuniversitario per la Fisica Spaziale) at the C3S Supercomputing Centre, Italy. The Jülich LOFAR Long Term Archive and the German LOFAR network are both coordinated and operated by the Jülich Supercomputing Centre (JSC), and computing resources on the supercomputer JUWELS at JSC were provided by the Gauss Centre for Supercomputing e.V. (grant CHTB00) through the John von Neumann Institute for Computing (NIC). This research made use of the University of Hertfordshire highperformance computing facility and the LOFAR-UK computing facility located at the University of Hertfordshire and supported by STFC [ST/P000096/1]. We thank the staff of the GMRT for making these observations possible. GMRT is run by the National Centre for Radio Astrophysics of the Tata Institute of Fundamental Research.

References

Bonafede, A., Brüggen, M., van Weeren, R., et al. 2012, MNRAS, 426, 40
Bonafede, A., Intema, H. T., Brüggen, M., et al. 2014, ApJ, 785, 1
Botteon, A., Gastaldello, F., Brunetti, G., & Kale, R. 2016, MNRAS, 463, 1534
Botteon, A., Brunetti, G., Ryu, D., & Roh, S. 2020, A&A, 634, A64
Botteon, A., Shimwell, T. W., Cassano, R., et al. 2022, A&A, 660, A78
Brunetti, G., & Jones, T. W. 2014, Int. J. Mod. Phys. D, 23, 1430007
Bykov, A. M., Vazza, F., Kropotina, J. A., Levenfish, K. P., & Paerels, F. B. S. 2019, Space Sci. Rev., 215, 14
Chandra, P., Ray, A., & Bhatnagar, S. 2004, ApJ, 612, 974
Chibueze, J. O., Akamatsu, H., Parekh, V., et al. 2023, PASJ, 75, S97
Condon, J. J., & Ransom, S. M. 2016, Essential Radio Astronomy (Princeton, NJ: Princeton University Press)
Condon, J. J., Cotton, W. D., Greisen, E. W., et al. 1998, AJ, 115, 1693
de Gasperin, F., Rudnick, L., Finoguenov, A., et al. 2022, A&A, 659, A146
Di Gennaro, G., van Weeren, R. J., Andrade-Santos, F., et al. 2019, ApJ, 873, 64
Dominguez-Fernandez, P., Bruggen, M., Vazza, F., et al. 2021, MNRAS, 500, 795
Domínguez-Fernández, P., Brüggen, M., Vazza, F., et al. 2021, MNRAS, 507, 2714
Domínguez-Fernández, P., Ryu, D., & Kang, H. 2024, A&A, 685, A68
Duchesne, S. W., Johnston-Hollitt, M., & Bartalucci, I. 2021, PASA, 38, e053
Ebeling, H., Edge, A. C., & Henry, J. P. 2001, ApJ, 553, 668
Edge, A. C., Ebeling, H., Bremer, M., et al. 2003, MNRAS, 339, 913
Ensslin, T. A., Biermann, P. L., Klein, U., & Kohle, S. 1998, A&A, 332, 395
Finner, K., HyeongHan, K., Jee, M. J., et al. 2021, ApJ, 918, 72
Golovich, N., Dawson, W. A., Wittman, D. M., et al. 2019, ApJ, 882, 69
Hindson, L., Johnston-Hollitt, M., Hurley-Walker, N., et al. 2014, MNRAS, 445, 330
Hoang, D. N., Shimwell, T. W., van Weeren, R. J., et al. 2018, MNRAS, 478, 2218

Hoeft, M., & Brüggen, M. 2007, MNRAS, 375, 77
Inchingolo, G., Wittor, D., Rajpurohit, K., & Vazza, F. 2022, MNRAS, 509, 1160
Intema, H. T., van der Tol, S., Cotton, W. D., et al. 2009, A&A, 501, 1185
Jaffe, W. J., & Perola, G. C. 1973, A&A, 26, 423
Jones, A., de Gasperin, F., Cuciti, V., et al. 2023, A&A, 680, A31
Kang, H., & Ryu, D. 2016, ApJ, 823, 13
Kang, H., Ryu, D., & Ha, J.-H. 2019, ApJ, 876, 79
Komissarov, S. S., & Gubanov, A. G. 1994, A&A, 285, 27
Markevitch, M., Govoni, F., Brunetti, G., & Jerius, D. 2005, ApJ, 627, 733
Navarro, J. F., Frenk, C. S., & White, S. D. M. 1997, ApJ, 490, 493
Offringa, A. R., & Smirnov, O. 2017, MNRAS, 471, 301
Offringa, A. R., McKinley, B., Hurley-Walker, N., et al. 2014, MNRAS, 444, 606
Owen, F. N., Rudnick, L., Eilek, J., et al. 2014, ApJ, 794, 24
Perley, R. A., & Butler, B. J. 2013, ApJS, 204, 19
Planck Collaboration XXVII. 2016, A&A, 594, A27
Rajpurohit, K., Hoeft, M., Vazza, F., et al. 2020, A&A, 636, A30
Rajpurohit, K., Wittor, D., van Weeren, R. J., et al. 2021, A&A, 646, A56
Rajpurohit, K., van Weeren, R. J., Hoeft, M., et al. 2022, ApJ, 927, 80
Rajpurohit, K., Lovisari, L., Botteon, A., et al. 2024, ApJ, 966, 38
Rengelink, R. B., Tang, Y., de Bruyn, A. G., et al. 1997, A&AS, 124, 259
Riseley, C. J., Scaife, A. M. M., Oozeer, N., Magnus, L., & Wise, M. W. 2015, MNRAS, 447, 1895
Roettiger, K., Burns, J. O., & Stone, J. M. 1999, ApJ, 518, 603
Rudnick, L., Katz-Stone, D. M., & Anderson, M. C. 1994, ApJS, 90, 955
Sarazin, C. L., Finoguenov, A., & Wik, D. R. 2013, Astron. Nachr., 334, 346
Shimwell, T. W., Markevitch, M., Brown, S., et al. 2015, MNRAS, 449, 1486
Shimwell, T. W., Röttgering, H. J. A., Best, P. N., et al. 2017, A&A, 598, A104
Shimwell, T. W., Tasse, C., Hardcastle, M. J., et al. 2019, A&A, 622, A1
Shimwell, T. W., Hardcastle, M. J., Tasse, C., et al. 2022, A&A, 659, A1
Skillman, S. W., Xu, H., Hallman, E. J., et al. 2013, ApJ, 765, 21
Stuardi, C., Bonafede, A., Rajpurohit, K., et al. 2022, A&A, 666, A8
Tasse, C., Shimwell, T., Hardcastle, M. J., et al. 2021, A&A, 648, A1
van Haarlem, M. P., Wise, M. W., Gunst, A. W., et al. 2013, A&A, 556, A2
van Weeren, R. J., Röttgering, H. J. A., Bagchi, J., et al. 2009, A&A, 506, 1083
van Weeren, R. J., Brüggen, M., Röttgering, H. J. A., & Hoeft, M. 2011, MNRAS, 418, 230
van Weeren, R. J., Bonafede, A., Ebeling, H., et al. 2012a, MNRAS, 425, L36
van Weeren, R. J., Röttgering, H. J. A., Intema, H. T., et al. 2012b, A&A, 546, A124
van Weeren, R. J., Brunetti, G., Brüggen, M., et al. 2016, ApJ, 818, 204
van Weeren, R. J., Ogrean, G. A., Jones, C., et al. 2017, ApJ, 835, 197
van Weeren, R. J., de Gasperin, F., Akamatsu, H., et al. 2019, Space Sci. Rev., 215, 16
van Weeren, R. J., Shimwell, T. W., Botteon, A., et al. 2021, A&A, 651, A115
Vazza, F., & Brüggen, M. 2014, MNRAS, 437, 2291
Vazza, F., Brüggen, M., van Weeren, R., et al. 2012, MNRAS, 421, 1868
Vazza, F., Brüggen, M., Wittor, D., et al. 2016, MNRAS, 459, 70
Wittor, D., Hoeft, M., Vazza, F., Brüggen, M., & Domínguez-Fernández, P. 2019, MNRAS, 490, 3987
Wittor, D., Brüggen, M., Grete, P., & Rajpurohit, K. 2023, MNRAS, 523, 701
Zhang, X., Simionescu, A., Stuardi, C., et al. 2021, A&A, 656, A59
Zhang, X., Simionescu, A., Gastaldello, F., et al. 2023, A&A, 672, A42
Zimbardo, G., & Perri, S. 2018, MNRAS, 478, 4922